Trends in Chemistry

CellPress

Review

Anomalous small-angle X-ray scattering for materials chemistry

Yugang Sun[1,*]

Over the past decade, the development of *in situ* characterization techniques has become necessary to understand the structure–property relationships of functional materials. *In situ* small-angle X-ray scattering (SAXS) represents one of the techniques for studying the evolution kinetics of materials structures, but the SAXS signals lack chemical information on the materials. Anomalous SAXS (ASAXS) measured at different energies near the X-ray absorption edge of an interesting element allows the deconvolution of element-specific SAXS profiles, enabling the promise of simultaneously revealing the evolution kinetics of both the structures and the chemistry of composite materials under operando conditions. Typical composite materials studied by ASAXS are overviewed to shed light on the potential of *in situ* ASAXS in materials chemistry research.

Highlights

Small-angle X-ray scattering (SAXS) is powerful method to determine the structures of interesting objects dispersed in a medium or nonuniform nanosized domains precipitated from a uniform matrix.

The differing energy dependences of the X-ray scattering factors of resonant elements and non-resonant elements in a composite sample support anomalous SAXS (ASAXS) measurement near the X-ray absorption edge of the resonant element, allowing the determination of element-specific structures.

ASAXS is suitable for studying multiconstituent systems involving phase separation, self-assembly, chemical interactions, and degradation/transformation of active components.

Both SAXS and ASAXS are suitable for *in situ* studies of the structure and chemistry of materials used in devices under operando conditions.

Principle of SAXS

SAXS (see Glossary) is a technique to probe the nonuniformity or discontinuity of the electron density of samples, allowing studies of the structure, geometry, size, size distribution, and interactions of small objects (e.g., atoms, ions, molecules, nanoparticles) dispersed in a medium [1,2]. Every atom in a sample reradiates (or scatters) a spherical wave upon interaction with the incident X-ray beam. The spherical waves interfere to generate an intensity pattern uniquely determined by the structural parameters of the sample. We can calculate the amplitude of the scattered wave by considering the phase differences between all waves scattered in a particular direction, commonly characterized by the momentum transfer $q = 4\pi \sin(\theta)/\lambda$, where 2θ and λ are the total scattering angle and the X-ray wavelength, respectively. Regular SAXS studies the elastic scattering of an X-ray beam with energy away from the absorption edges of the sample elements into angles of only a few degrees with respect to the forward direction of the incident beam (Figure 1A, top). In the small-angle regime of interest, the scattering amplitude $A\left(\vec{q}\right)$ of a sample is computed from the collection of N atoms:

$$A\left(\vec{q}\right) = \sum_{n=1}^{N} e^{i\vec{q}\vec{r}_n} f_n\left(\vec{q}\right). \quad [1]$$

The position and scattering factor of the nth atom are denoted r_n and $f_n\left(\vec{q}\right)$, respectively. The intensity, $I(q)$, measured by the experiment is computed from the multiplication of $A\left(\vec{q}\right)$ and its **complex conjugate**; that is, $I(q) = A\left(\vec{q}\right) \times A^*\left(\vec{q}\right) = \left|A\left(\vec{q}\right)\right|^2$. The scattering factor of one atom depends on its type, which determines the electron density and the energy of X-ray absorption photons. For example, nanoparticles or macromolecules dispersed in a liquid solvent exhibit electron densities different from the background solvent. The nonuniform electron density in the solution enables the observation of distinguished SAXS signals from the nanoparticles or macromolecules. Since the waves scattered from all atoms exhibit the same phase in the forward

[1]Department of Chemistry, Temple University, Philadelphia, PA 19122, USA

*Correspondence:
ygsun@temple.edu (Y. Sun).

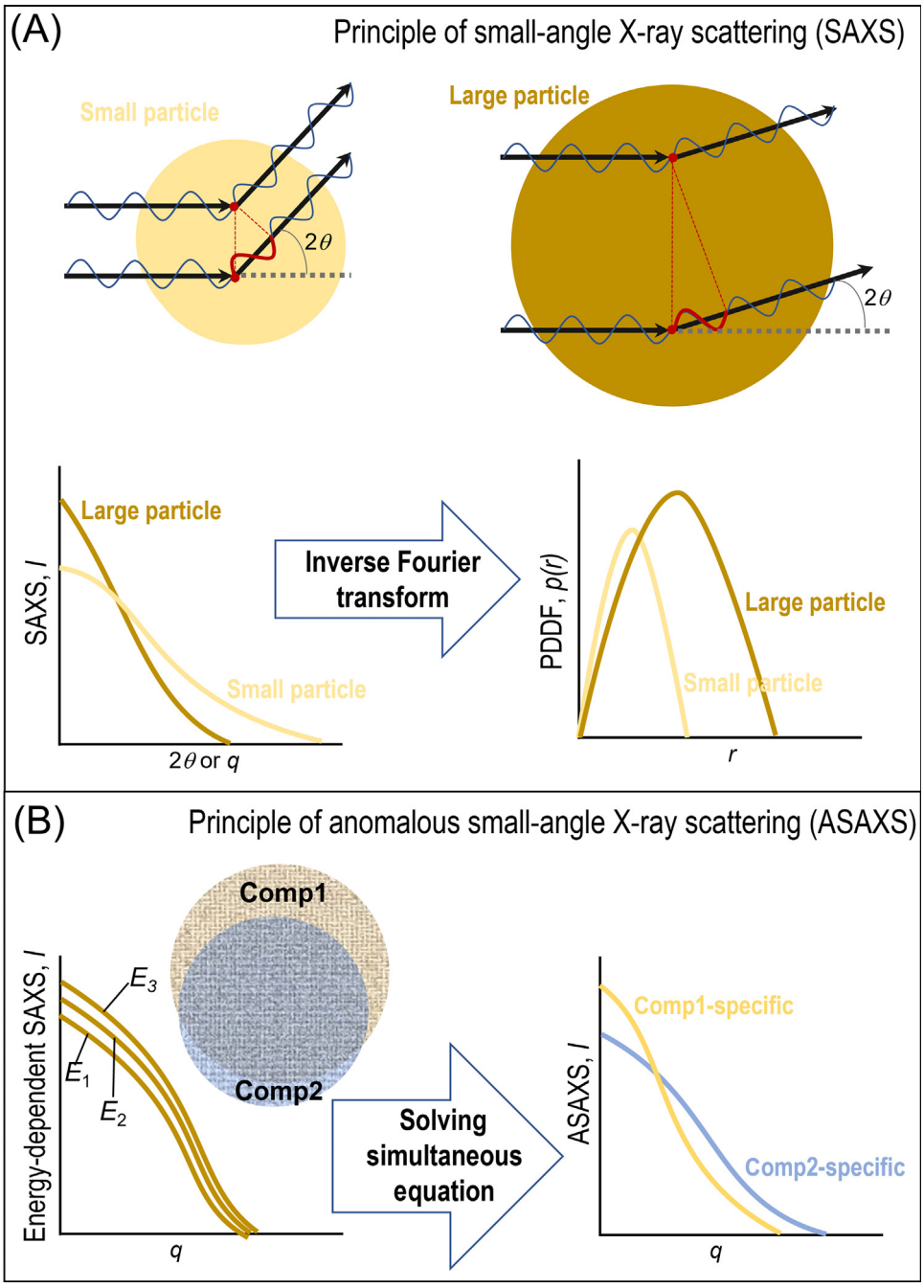

Figure 1. Schematic illustrations of the working principles for (A) small-angle X-ray scattering (SAXS) and (B) anomalous SAXS (ASAXS). (A) A SAXS profile in the **reciprocal space** is sensitive to the size and mass distribution (or structure) of an object and the inverse Fourier transform of the SAXS profile gives a pair distance distribution function (PDDF) profile in the real space. (B) Measurement of SAXS profiles at different energies near the **X-ray absorption edge** of one element results in a simultaneous equation, which can be solved to deconvolute the energy-independent element-specific SAXS profiles to study both the structures and the chemistry of a composite material.

Glossary

Anomalous small-angle X-ray scattering (ASAXS): SAXS showing energy-dependent intensity using the incident X-ray with energy near the absorption edge of a targeted element.
Block copolymer (BCP): a polymer comprising two or more homopolymer subunits linked by covalent bonds.
Block copolymer micelles: one type of micelle formed from the self-assembly of either amphiphilic or oppositely charged BCPs.
Complex conjugate: a mathematical term of a complex number; a complex conjugate of a complex number referring to the number with an equal real part and an imaginary part equal in magnitude but opposite in sign.
Guinier formula: an equation transforming the Guinier region in SAXS, which defines the radius of gyration and the forward scattering intensity, into a characteristic peak for visual and automated inspection of data.
Indirect Fourier transform: a solution of the problem involving the Fourier transform of a function with known variables in a definite range, which is common in experimental data.
Kramers–Kronig relation: a bidirectional mathematical relation connecting the real and imaginary parts of any complex function, which is often used to compute the real part from the imaginary part (or vice versa) of a response function in a physical system.
Non-resonant element: an element measured using the incident X-ray with energy (far) away from its X-ray absorption edges.
Pair distance distribution function (PDDF): a measure of the frequency of interatomic vector lengths in a molecule/nanoparticle that can provide information about the shape of the molecule/nanoparticle.
Reciprocal space: a frequency domain to visualize the results of the Fourier transform of a spatial function.
Resonant element: an element measured using the incident X-ray with energy near its X-ray absorption edge.
Small-angle X-ray scattering (SAXS): a technique to quantify nanoscale differences of electron density (or mass density) using the intensity profile of X-rays scattered in small angles.
X-ray absorption edge: sharp absorption discontinuity in the X-ray absorption spectrum of an element.

direction (i.e., $q = 0$), $I(q{=}0)$ or I_0 is proportional to the square of the total number of electrons in the sample. As the scattering angle slightly increases, the scattering intensity from a larger object falls off more rapidly than the scattering intensity from a smaller object because of the greater different path lengths (corresponding to phase) of the scattered X-rays (Figure 1A, bottom left). The shape of the SAXS profile reflects the arrangement (or structure) of the scattering unit within the interesting objects.

X-ray scattering factor: a measure of the scattering power of a scattering unit (e.g., atom, molecule, nanoparticle) that can be evaluated as the Fourier transform of the electron-density distribution.

In a dilute system with negligible intermolecular/interparticle interference, the SAXS profile is described by the **Guinier formula**:

$$I(q) \approx I_0 \exp\left(-q^2 R_g^2/3\right), \quad [2]$$

where R_g is a model-free characterization of the molecule/particle size and I_0 is related to the weight of a molecule/particle. When the intermolecular/interparticle interference cannot be ignored or the molecules/particles condense into clusters, a more general SAXS profile can be written in terms of the distribution function $p(r)$ of the intramolecular/intraparticle atomic distance:

$$I(q) = \int_0 d\vec{r}\, p\left(\vec{r}\right) \frac{\sin\left(\vec{q}\,\vec{r}\right)}{\vec{q}\,\vec{r}}, \quad [3]$$

with D_{max} representing the maximum intramolecular/intraparticle distance. An **indirect Fourier transform** of the SAXS profile using software such as GNOM [3,4] or GIFT (generalized indirect Fourier transformation) [5] derives the **pair distance distribution function (PDDF)**, $p\left(\vec{r}\right)$, providing the structural information of the molecules/particles in the real space. For instance, the use of $p\left(\vec{r}\right)$ to help visualize molecular shape has been superseded by algorithms that provide a 3D electron density map of the molecule from the 1D SAXS profile. The physical 3D geometry of molecules can also be reconstructed from the 1D SAXS profile using the *ab initio* determination protocol, in which an appropriate assembly of beads or dummy atoms renders the molecule. The reconstruction can be numerically realized using various Monte Carlo-like procedures, including Chacon's method (termed Dalai GA) using a genetic algorithm [6], DAMMIN using a simulated annealing process [7], GASBOR [8], and saxs3d using a 'give-'n'-take' algorithm [9]. The advance of technical development and detectors enables the high-resolution measurement of SAXS signals at low q, which helps to extend SAXS to the study of nanoparticles, including 3D geometrical reconstruction (or imaging) [10]. However, the regular SAXS profile cannot distinguish the structure (e.g., spatial distribution) of the different elements in composite samples containing multiple compositions; for example, alloy nanoparticle catalysts.

ASAXS adding chemical information to structure

The scattering factor of a given atom also depends on the X-ray energy (E), particularly near the absorption edge of the element, at which resonant scattering occurs. The complex quantity of the **X-ray scattering factor** of a **resonant element** (labeled as subscript R) is described by

$$f_R(E) = f_{0,R} + f'_R(E) + i f''_R(E). \quad [4]$$

$f_{0,R}$ is the scattering factor at X-ray energy far from the absorption edge, at which the SAXS signal originates from the non-resonant scattering. The real and imaginary parts (f' and f'') are the dispersion corrections independent of q but strongly dependent on the X-ray energy. According to the **Kramers–Kronig relation**, f' and f'' are related, and the tabulated values as a function of energy are available for most elements [11]. In practical data analysis, it is strongly recommended to

convolute the tabulated values with the actual energy resolution $\Delta E/E$ of the instrument or determine it *in situ* from the absorption coefficient of standard samples. Figure 2 presents the theoretical absorption edges of some elements in the energy range 7–17 keV [12], highlighting how significantly f' and f'' vary near the absorption edges. The real part (f') of an element becomes more negative and its imaginary part (f'') becomes more positive at the absorption edge. The variation of f at different X-ray energies can be transferred to the variation of total SAXS profiles when a sample is studied at a number of energies near the absorption edge of a specific element, enabling the feasibility of **ASAXS** (Figure 1B).

Performing ASAXS measurements on multicomponent samples in the vicinity of the absorption edge of one interesting element gives the energy-dependent total scattering intensity,

$$I_{\text{tot}}(q,E) = \left|A_R(\vec{q},E) + A_{NR}\left(\vec{q},E\right)\right|^2 = \left|A_R\left(\vec{q},E\right)\right|^2 + \left|A_{NR}\left(\vec{q},E\right)\right|^2 + 2\left[A_R\left(\vec{q},E\right)\cdot A_{NR}(\vec{q},E)\right], \quad [5]$$

in which the subscripts R and NR stand for the interesting element with resonant scattering and for all of the other components in the sample with non-resonant scattering, respectively. The first two terms, $\left|A_R\left(\vec{q}\right)\right|^2$ and $\left|A_{NR}\left(\vec{q}\right)\right|^2$, are the autocorrelation of the electron densities within the resonant element and the non-resonant constituents, respectively. The third term,

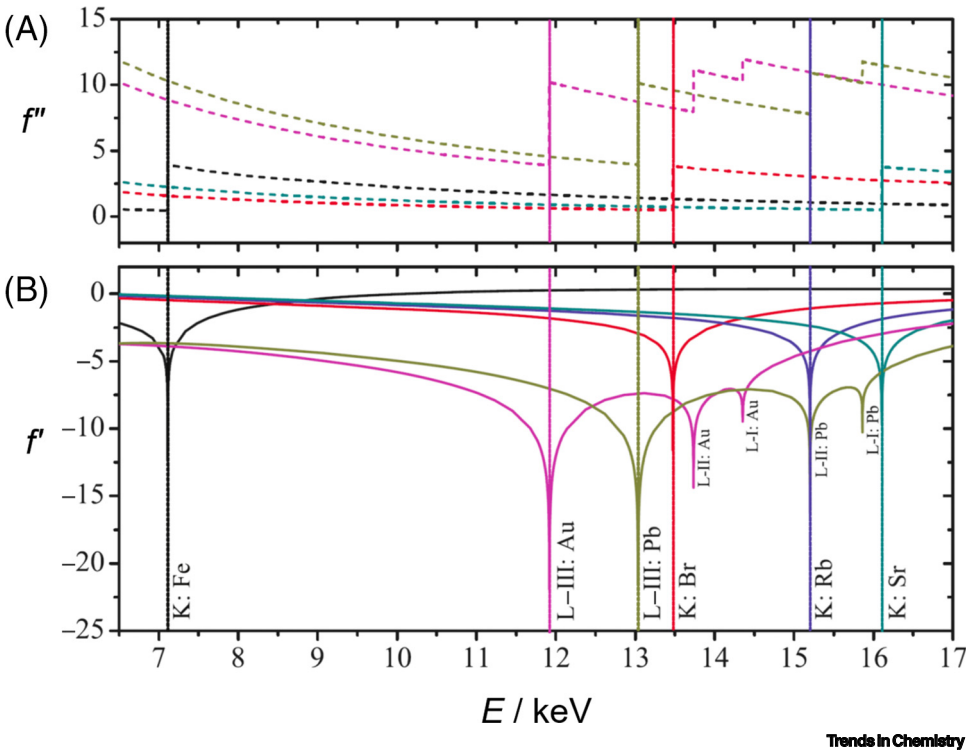

Figure 2. Dependence of the real part (f') and imaginary part (f'') of the X-ray scattering factor (f) on the X-ray energy for typical elements with absorption edges in the range 7–17 keV. The absorption edges accessible in this range include the *K*-edges of some main-group elements (e.g., Fe, Br, Rb, Sr) and the *L* edges of some heavy elements (e.g., Au, Pb). The vertical lines highlight the abrupt changes of f' and f'' at the absorption edges, which are responsible for the anomalous effect in anomalous small-angle X-ray scattering (ASAXS) measurements. Adapted from [12].

$2\left[A_R\left(\vec{q}\right) \cdot A_{NR}\left(\vec{q}\right)\right]$, is the cross-term originating from the superposition of the scattering amplitudes of the resonant and non-resonant scattering atoms. The superposition can be expressed as the Fourier transform of the correlation function of the electron densities:

$$A_R\left(\vec{q}\right) A_{NR}\left(\vec{q}\right) = \int_0^{D_{\max,NR}} \int_0^{D_{\max,R}} \rho_R(\vec{r}_R)\ \rho_{NR}(\vec{r}_{NR}) e^{-i\vec{q}\left(\vec{r}_R - \vec{r}_{NR}\right)} d\vec{r}_R^{\,3} d\vec{r}_{NR}^{\,3}. \quad [6]$$

The cross-term not only contains information on the electron density variation of the resonant and non-resonant atoms normalized against the background matrix ($\Delta\rho_R$ and $\Delta\rho_{NR}$) but also includes their spatial positional relationship, which is expressed by $e^{-i\vec{q}\left(\vec{r}_R - \vec{r}_{NR}\right)}$. This cross-term is not always as positive as the other two terms. Equation 5 can be rewritten as a combination of the scattering signals of each term I_i [including the resonant element-specific SAXS profile, $I_R(q)$] with their electron density contrasts $\Delta\rho$ as coefficients:

$$I_{\text{tot}}(q,E) = \rho_R{}^2\, I_R(q) + \rho_{NR}{}^2\, I_{NR}(q) + 2\,\rho_R\ \rho_{NR}\, I_{R,NR}(q). \quad [7]$$

In a typical ASAXS measurement, a series of SAXS profiles are measured at different X-ray energies near the absorption edge of one element at which its effective electron density ρ dramatically changes, by following

$$\rho_R \propto f_R(q,E) = f_{0,R}(q) + f'_R(E) + i f''_R(E). \quad [8]$$

Therefore, we can deconvolute the resonant element-specific SAXS profile [i.e., $I_R(q)$ independent of E] from ASAXS measurements by solving the simultaneous equation of a set of Equation 7 ($n \geq 3$) [13]:

$$\begin{cases} I_{\text{tot}}(q,E_1) = f_R{}^2(E_1) I_R(q) + f_{NR}{}^2(E_1) I_{NR}(q) + 2\ f_R(E_1)\ f_{NR}(E_1) I_{R,NR}(q) \\ I_{\text{tot}}(q,E_2) = f_R{}^2(E_2) I_R(q) + f_{NR}{}^2(E_2) I_{NR}(q) + 2\ f_R(E_2)\ f_{NR}(E_2) I_{R,NR}(q) \\ \cdots \\ I_{\text{tot}}(q,E_n) = f_R{}^2(E_n) I_R(q) + f_{NR}{}^2(E_n) I_{NR}(q) + 2\ f_R(E_n)\ f_{NR}(E_n) I_{R,NR}(q) \end{cases}. \quad [9]$$

Equation 9 can be simplified using the following vector equation:

$$\overset{\boldsymbol{X}}{\begin{bmatrix} f_R{}^2(E_1) & f_{NR}{}^2(E_1) & 2\ f_R(E_1)\ f_{NR}(E_1) \\ f_R{}^2(E_2) & f_{NR}{}^2(E_2) & 2\ f_R(E_2)\ f_{NR}(E_2) \\ \vdots & \vdots & \vdots \\ f_R{}^2(E_n) & f_{NR}{}^2(E_n) & 2\ f_R(E_n)\ f_{NR}(E_n) \end{bmatrix}} \overset{\boldsymbol{\beta}}{\begin{bmatrix} I_R(q) \\ I_{NR}(q) \\ I_{R,NR}(q) \end{bmatrix}} = \overset{\boldsymbol{y}}{\begin{bmatrix} I_{\text{tot}}(q,E_1) \\ I_{\text{tot}}(q,E_2) \\ \vdots \\ I_{\text{tot}}(q,E_n) \end{bmatrix}}. \quad [10]$$

The first matrix, $\boldsymbol{X}$ is the design matrix because it contains all of the explanatory variables. The second vector/matrix, denoted $\boldsymbol{\beta}$, contains the unsolved element-specific and cross-term SAXS profiles. The vector/matrix $\boldsymbol{y}$ on the right side is experimental measurements at n different X-ray energies. The ASAXS problem becomes solving $\boldsymbol{\beta}$ with the knowledge of $\boldsymbol{X}$ and $\boldsymbol{y}$. Although $f_0(q)$ gradually drops from low q to high q [14], its variation can be essentially ignored in a typical SAXS measurement that is performed in a narrow range of q (typically $q < 1.0$ Å^{-1}). The real part, $f'_R(E)$, and the imaginary part, $f''_R(E)$, in $\boldsymbol{X}$ can be computed from Kramers–Kronig relation

or experimentally determined from *in situ* measurements of standard samples. The accuracy of f_R at different energies should be high enough to echo the variation of recorded I_{tot}, enabling the feasibility of solving the element-specific $I_R(q)$ with reasonable fidelity. If the sample comprises the resonant element and another **non-resonant element**, the ASAXS measurement near the absorption edge of the resonant element can simultaneously solve the element-specific SAXS profiles $I(q)$ for both elements (Figure 1B). If the sample comprises three or more elements, ASAXS measurements near the absorption edge of each interesting element should be performed to achieve the element-specific SAXS profiles.

The availability of the element-specific SAXS profiles of a composite sample allows studies of the structures with chemical specificity, as discussed in the previous section. Therefore, ASAXS represents an advanced technique promising for the investigation of high-resolution structures of composite samples with chemical specificity. Recent developments in synchrotron light sources and detectors and the ability of more researchers to access beamline facilities promote the application of ASAXS in a broad range of materials chemistry, including *in situ* studies under operando conditions. This short review summarizes the typical material systems that have been examined by the emerging ASAXS back to 2013. *In situ* ASAXS studies of working energy devices (e.g., batteries, supercapacitors, catalytic reactors) are highlighted to demonstrate the feasibility and promise of *in situ* ASAXS in probing the structural evolution kinetics of functional materials with element specificity. The review concludes with challenges and personal perspectives on the future research directions.

Composite material systems studied with ASAXS

Composite samples containing elements that exhibit spatial discontinuity can be theoretically studied with ASAXS when the experimental setup can reach the absorption edges of the interesting elements. According to the physical and chemical states, the composite materials and phenomena studied with ASAXS are classified into four categories.

Nanophase separation in solids

When a composite solid undergoes treatment with external stimuli such as thermal annealing and irradiation, phase segregation and element redistribution may occur (Figure 3). The resulting nanoscale (crystalline) phases with compositions differing from the surrounding solid matrix can be studied with ASAXS. For example, thermal annealing of amorphous silicate glass with a composition of $1.88Na_2O{\cdot}15.04K_2O{\cdot}7.52Al_2O_3{\cdot}69.56SiO_2{\cdot}6.00BaF_2$ (wt%) at 580°C led to the formation of cubic BaF_2 nanocrystals in the glass matrix. ASAXS studies near the Ba L_{III} edge reveal that the BaF_2 nanocrystals possess sizes in the nanometer range and are surrounded by nanoshells comprising a lower-electron-density glass [15,16]. The depleted nanoshells behave like a diffusion barrier to hinder the growth of BaF_2 nanocrystals. The phase separation (crystalline versus amorphous) is a solid process, but liquid/liquid phase separation of droplets with sizes of around 100 nm occurs when the glass is doped with a trace amount of SmF_3 (0.05%). A similar thermally induced crystalline phase separation of forming core-shell nanostructures also occurs in other silicate glasses [17,18]. Composition-distinguished oxide nanoclusters embedded in oxide films have been studied with anomalous grazing-incidence SAXS to analyze their geometry and size. Examples include Ga_2O_3 nanoparticles embedded in In_2O_3 films [19] and self-organized nanoclusters (e.g., Zn-rich nanoclusters, Ga-rich nanoclusters) formed from solution-processed mesoporous In-Ga-Zn-O films [20]. ASAXS was also used to study the formation and existence of element-specific nanodomains in alloys [21–24]. *In situ* ASAXS studies on the strain glass transition (SGT) in as-quenched $Ti_{48.7}Ni_{51.3}$ shape-memory alloy determine the distribution of Ni atoms in nanodomains, which exhibit a disk-like core-shell configuration with a Ni-rich shell and

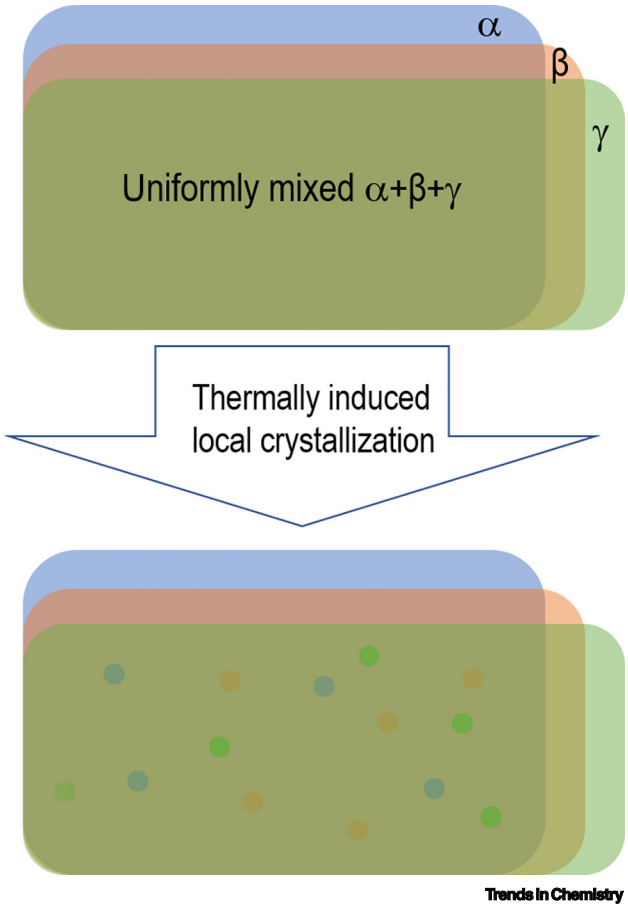

Figure 3. Schematic illustration of the formation of crystallized nanodomains in a composite solid comprising multiple constituents (α, β, γ) on an external stimulus (e.g., thermal annealing). The crystalline nanodomains exhibit nonuniform mass distribution (as indicated by colored dots) compared with the surrounding solid matrix, resulting in discontinuities of electron density in the composite solid.

a highly Ni-rich core [21]. Additional composite solids studied by ASAXS include nanophase precipitates in oxide dispersion-strengthened (ODS) steels [25,26], superconductor tapes [27], and hydrogen-storage materials [28–30].

Counterions in charged macromolecules

Interactions between charged molecules and counterions are essential to determine their structures and solution behaviors. ASAXS measurements near the absorption edge of counterions provide a strategy to study their spatial distributions near/in charged macromolecules at nanometer resolution. Figure 4A illustrates the distribution of counterions around a structurally rigid and well-defined macroion, $\{[Mo^{VI}(Mo^{VI}_5O_{21})(H_2O)_6]_{12}[Mo^{V}_2O_4(CH_3COO)]_{30}\}^{42-}$, or $\{Mo_{132}\}^{42-}$, with spherical geometry and a diameter of 2.9 nm. The skeleton of $\{Mo_{132}\}^{42-}$ carries 12 negative charges and 30 negative acetate ligands coordinating to the skeleton stay inside. ASAXS was applied to determine the accurate distribution of both monovalent and divalent cations (i.e., Rb^+ and Sr^{2+}) around $\{Mo_{132}\}^{42-}$ in an aqueous solution [31]. Both Rb^+ and Sr^{2+} ions lead to thinner diffuse layers around $\{Mo_{132}\}^{42-}$ than theoretical expectation. The monovalent Rb^+ ions favor close association with $\{Mo_{132}\}$ by staying near the skeleton (i.e., in the Stern layer), while divalent Sr^{2+} ions loosely associate with $\{Mo_{132}\}$ in the diffuse layer. The difference of their spatial distributions indicates the stronger affinity of Rb^+ towards $\{Mo_{132}\}$, which explains the lower critical coagulation concentration of $\{Mo_{132}\}$ with Rb^+ compared with Sr^{2+}. In another study, combining ASAXS with X-ray absorption fine spectroscopy (XAFS) determined the location

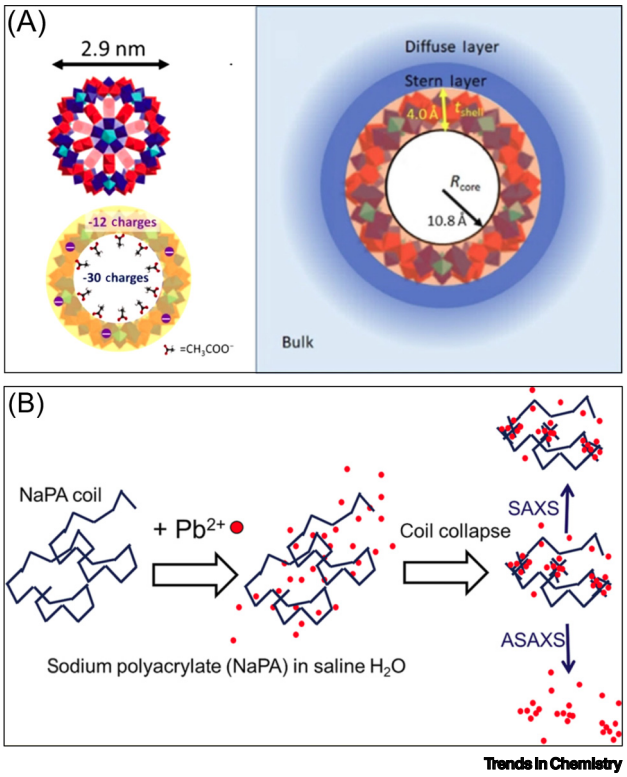

Figure 4. Schematic illustration of composite systems of macromolecules interacting with counterions. (A) Structure (top left) and charge distribution (bottom left) of an inorganic macromolecule (or macroion) of $\{Mo_{132}\}$ with rigid structure and spherical geometry. The drawing on the right represents the multilayered model with counterions in both the Stern layer and the diffuse layer used for fitting the small-angle X-ray scattering (SAXS) profiles of specific counterions (e.g., Rb^+ and Sr^{2+}) deconvoluted from the anomalous SAXS (ASAXS) measurement. Adapted from [31]. (B) Structural collapse of flexible polyacrylate coils upon interaction with counterions (e.g., Pb^{2+}) in saline. SAXS signals include contributions from both polyacrylate coils and Pb^{2+} ions. ASAXS measurement near the absorption edge of Pb can extract the element-specific SAXS profile to determine the spatial distribution of Pb^{2+} ions in the polyacrylate coils. Adapted from [33].

of Cu^{2+} in silicoaluminophosphate (SAPO-5) frameworks, one type of molecular sieve. Hydrothermal crystallization favors the location of Cu^{2+} ions at the inner and outer surfaces of the framework, exhibiting high thermal stability in an argon (Ar) atmosphere up to 550°C. By contrast, Cu^{2+} deposited by impregnation on a pure SAPO-5 framework can be easily reduced to Cu^+ in Ar [32].

Charged organic macromolecules are mechanically flexible, and their geometrical configurations change upon interaction with counterions. For example, highly charged water-soluble polymer chains (or polyelectrolytes) are sensitive to solvents and salt additives. Sodium polyacrylate (NaPA), one of the widely studied polyelectrolyte chains, exhibits specific interactions with alkaline-earth cations, heavy-metal cations, and some transition-metal cations. This property renders NaPA a candidate to be used as an antiscalant or additive in water-desalination processes. The interactions lead to significant changes in the conformation of NaPA coils, implying relevance for the development of new responsive materials. The specific interactions of divalent lead cations (Pb^{2+}) with the negatively charged COO^- residues of NaPA chains in dilute aqueous solution eventually result in the aggregation and precipitation of NaPA chains (Figure 4B). SAXS studies reveal that the NaPA coils collapse as the concentration of Pb^{2+} reaches the precipitation threshold. ASAXS measurements near the Pb L_{III} absorption edge provide insight into the spatial distribution of Pb^{2+} cations captured by NaPA chains and semiquantitative estimation of the amount of Pb^{2+} cations trapped within the collapsed domains [33]. The partially collapsed coils exhibit pearl-like subdomains with a size on the order of a few nanometers [34]. Cation-induced aggregation of azo dyestuffs in dilute aqueous solution forms a gel phase comprising a network of partial lateral alignment of the dyestuff fibers. ASAXS analysis of a gel formed on the addition of Sr^{2+} reveals the extent of neutralization of the dyestuff molecules in the gel [35].

Most biomolecules possess negatively charged chains and can interact with counter cations to change the geometrical configurations that determine their biological activities. ASAXS has been extensively used to investigate the interactions and spatial distribution of cations in biological molecules/assemblies including DNA [36–41], proteins [41,42], and membranes [43]. When the ends of biological molecules are precisely labeled with Au nanoparticles, ASAXS measurements near the Au L_{III} absorption edge allow accurate determination of the intermolecular distance of DNA constructs [44,45].

Block copolymer (BCP) micelles

Micelles self-assembled from amphiphilic **BCPs** with hydrophilic and hydrophobic (or lipophilic) block groups in aqueous solutions represent a class of typical materials widely investigated by ASAXS. ASAXS measurements with the assistance of appropriate marker elements (e.g., Br and Rb) can determine the structure of micelles and the distribution of interesting molecules encapsulated in the micelles (Figure 5). Figure 5A shows the micelles formed from poly(4-vinylphenol rubidium salt)-*block*-poly(4-bromostyrene) (RbPVPh-*b*-PBrS), in which Br and Rb serve as the makers for ASAXS measurements at their *K* absorption edges [46]. Since Br and Rb locate in the hydrophobic and hydrophilic blocks, respectively, their spatial distributions indicate the core-shell structure of the micelles. Each micelle is constructed with a hydrophobic PBrS core and hydrophilic hydrated PVPh corona shell. The core is a solid sphere with a smooth surface and a radius of 47 nm and the shell exhibits a thickness of 15 nm. If BCP molecules lack appropriate marker elements, the spatial distribution of functional groups such as hydrophilic COO^- groups in micelles can be studied by probing counterions that can interact with the functional groups. For instance, Rb^+ and Sr^{2+} cations combined with ASAXS were used to probe the COO^- groups of sophorolipid micelles, revealing that the COO^- groups spread in the broad hydrophilic shell rather than at the outer micellar/water interface [47].

BCP micelles represent a class of unique carriers for drugs stored in the hydrophobic core and gradually released into the hydrophilic environment. Hydrophobic molecules mimicking general drugs have been used as models to evaluate the spatial distribution of the molecules encapsulated in micelles. Figure 5B presents the ASAXS measurement on the distribution of hydrophobic compound tetrabromocathecol (TBC) in the core-shell micelles of poly(ethylene glycol)-*block*-poly(partially benzyl-esterified aspartic acid) {PEG-P[Asp(Bzl)] or PEAB} [48]. The results indicate that the TBC molecules infiltrate the PEG hydrophilic domain in the vicinity of the core/shell interface. The infiltration of TBC into the hydrophilic shell is ascribed to the hydrophilicity of -OH groups in TBC. Comparative studies on bromobenzene (BrBz) and 4-bromophenol (BrPh) in poly(ethylene glycol)-*block*-poly(*tert*-butyl methacrylate) (PEG-*b*-PtBMA) micelles [49] as well as BrBz and 4-bromobenzylalcohol (BrBzOH) in poly(*N*,*N*-dimethylaminoethyl methacrylate)-*block*-poly(methyl methacrylate) (PDMAEMA-*b*-PMMA) micelles [50] show that all of the small molecules homogeneously disperse in the hydrophobic micelle cores. BrBz molecules are exclusively confined in the hydrophobic cores, but BrPh and BrBzOH molecules containing -OH groups also exist in the hydrophilic shells at low concentrations. Large hydrophobic molecules such as homopolymers behave differently from the small molecules upon loading them in BCP micelles. Figure 5C summarizes the ASAXS results for the distribution of poly(4-hydroxystyrene) brominated (Br-PHS) in the cylindrical core-shell micelles of polystyrene-*block*-poly(4-hydroxystyrene) (PS-PHS) on a silicon substrate [51]. Br-PHS molecules segregate to the PS-PHS interface to stabilize the micelles by reducing the interfacial energy of the PS shells and PHS cores.

The process of determining element-specific structures and dimensions from typical ASAXS measurements is highlighted using the example shown in Figure 5B [48]. In this study, the

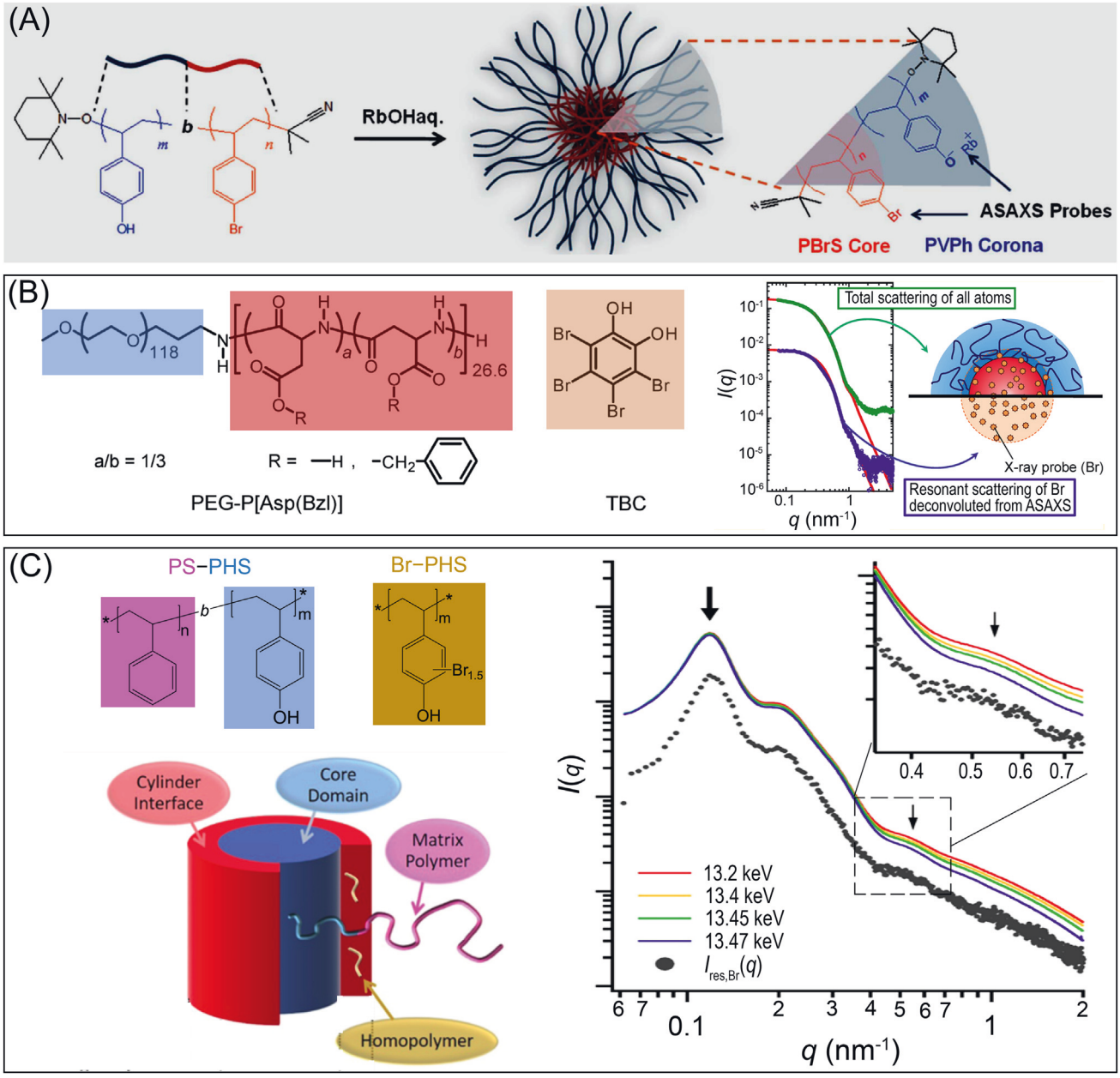

Trends in Chemistry

Figure 5. Schematic illustration of (A) block copolymer micelle formation and the distribution of (B) small molecules and (C) large polymer molecules in micelles. (A) Self-assembly of poly(4-vinylphenol rubidium salt)-*block*-poly(4-bromostyrene) into spherical core-shell micelles with solid hydrophobic cores and corona-type hydrophilic shells in aqueous solution. Adapted from [46]. (B) Spatial distribution of tetrabromocatechol (TBC) molecules in the core-shell micelles of poly(ethylene glycol)-*block*-poly(partially benzyl-esterified aspartic acid) formed in aqueous solution. The total small-angle X-ray scattering (SAXS) profile of all atoms of the micelles is compared with the resonant scattering profile of Br that is deconvoluted from the anomalous SAXS (ASAXS) measurement. Adapted from [48]. (C) Spatial distribution of poly(4-hydroxystyrene) brominated (Br-PHS) in the cylindrical core-shell micelles of polystyrene-*block*-poly(4-hydroxystyrene) (PS-PHS) formed on a silicon substrate in air. ASAXS measurement of the micelles near the X-ray absorption *K*-edge of Br (unbroken curves) and the resonant scattering profile of Br deconvoluted from the ASAXS measurement (symbols). The thick and thin arrows highlight the scattering peaks and humps that are attributed to the interparticle and intraparticle interfaces, respectively. Adapted from [51].

average number of aspartic units and the benzyl esterified molar ratio in PEAB are determined to 26.9 and 83.3 mol% (denoted PE-A27-B83), respectively, according to ^{1}H NMR characterizations. The critical micellar concentration (CMC) of PE-A27-B83 is 2.2 μg/ml, which is lower than those used in all of the SAXS measurements. The PEAB micelles with different loadings of TBC (w_{TBC} = 0, 1.6, 2.4, and 4.0 wt%) are denoted PEAB-0, PEAB-Br1.6, PEAB-Br2.4, and PEAB-Br4.0, respectively. SAXS profiles of PEAB micelles with a low concentration (c) are recorded at an X-ray energy (E_0 = 12.4 keV) far below the absorption edge of Br (13.386 keV). Figure 6A compares the SAXS profiles [i.e., $I(q, E_0, 0)/c$ (representing the intensity at the infinite dilution limit)], as a function of q, of TBC-free and TBC-loaded PEAB micelle solutions. These SAXS profiles exhibit major features, including the minor dependence of I at low q, significant dependence at intermediate q, and two maxima at high q. The presence of the second maximum at $q \approx 3.5$ nm^{-1} indicates the morphological uniformity and narrow size distribution of the micelles. A theoretical model of core-shell morphology is used to fit the measured SAXS profiles, resulting in the theoretical curves (Figure 6A, solid red curves). The deviation of the theoretical curves indicates the atomic-scale density fluctuation of the core-constituting chains (i.e., the edge of the amorphous halo) and/or the conformational fluctuation of the shell chains. Despite the high sensitivity of SAXS at the non-resonant X-ray energy, the SAXS signals are usually attenuated at X-ray energy near the absorption edge of an interesting element (e.g., Br). It becomes necessary to increase the concentration of micelles in ASAXS measurements to achieve decent signal-to-noise ratios. However, the intermicelle interference at high concentrations changes the typical features of scattering profiles (Figure 6B, top). The concentration-dependent interference can be described by a structure factor that is determined by dividing $I(q, E_0, 40)/c$ (at c = 40 mg/ml) by $I(q, E_0, 0)/c$ (at c close to zero) (Figure 6B, bottom frame). The structural factor at c = 40 mg/ml is energy independent and applicable for the SAXS profiles measured at any X-ray energy. The left frame of Figure 6C presents SAXS profiles of PEAB-Br2.4 micelles at 40 mg/ml concentration recorded at several X-ray energies near the absorption edge of Br, which can be corrected to give typical SAXS profiles by applying the structural factor (i.e., the typical ASAXS profile; Figure 6C, right frame). Solving Equation 10 gives a plot of the concentration-normalized square of the volume $[v^2(q)/c]$ of only Br as a function of q (Figure 6D, blue symbols). The plot is consistent with that of a spherical object with a maximum radius of 4.8 ± 0.1 nm, which is larger than the core radius (4.5 ± 0.1 nm) of the micelles determined from analysis of a typical SAXS profile (Figure 6D, black symbols). The dimensional difference confirms the infiltration of TBC molecules into the PEG hydrophilic shells in the vicinity of the core/shell interface (Figure 6E).

Supported nanoparticle catalysts and dispersed multi-element nanoparticles

The power of ASAXS can benefit the study of catalyst nanoparticles on complex supports (Figure 7A) by measuring SAXS profiles near absorption edges of the catalysts, providing detailed structural information on the catalyst nanoparticles with minimization of the background interference of the supports. Typical examples are composite catalysts including MoS_2 nanoparticles in sulfide slabs [52], MnO_2 nanoparticles on carbon xerogel [53], ceria nanoparticles on nanoporous gold [54], Pt nanoparticles on oxides [55] and mesoporous MCM-41 silica [56], Pt(Ni) nanoparticles on TiO_2 or TiO_2/C supports [57], Co nanoparticles on γ-alumina [58], Ni and Ni-alloy nanoparticles in zirconia matrix [59], and Ni nanoparticles on spinel $MgAl_2O_4$ [60]. When nanoparticles have multiple compositions, individual elements may distribute differently to form different structures (Figure 7B). The element specificity of ASAXS allows rendering of the structures of multicomposition nanoparticles such as Au/Pd nanoparticles [61], Ru@Cu [62], CdSe@CdS [63], and Fe_3O_4@γ-Mn_2O_3 core-shell nanoparticles [64]. ASAXS together with a complementary technique has also been applied to nonspherical nanoparticles with gradient compositions [65].

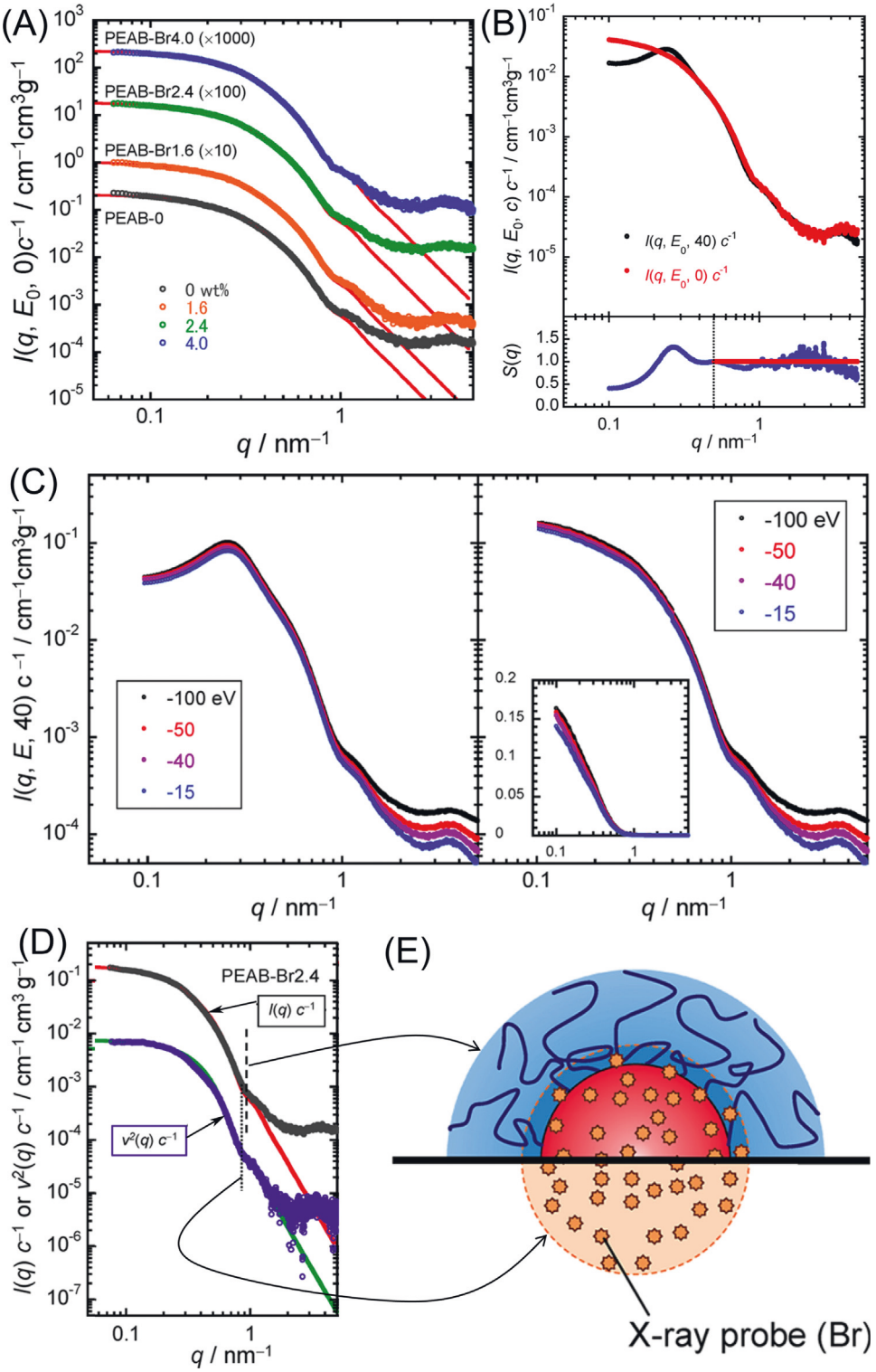

Trends in Chemistry

(See figure legend at the bottom of the next page.)

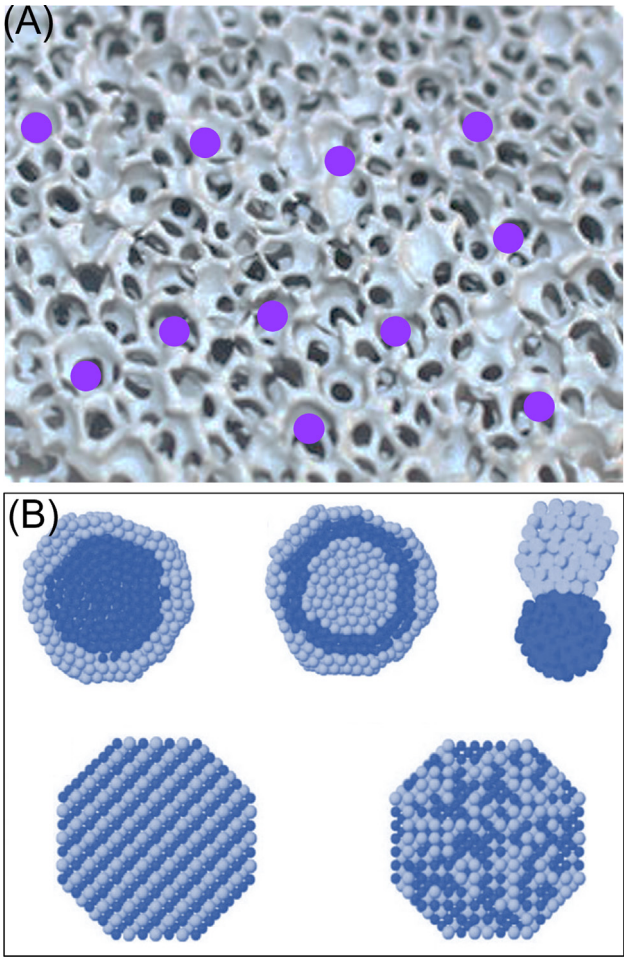

Figure 7. Schematic illustration of (A) catalyst nanoparticles on porous support with complex structure and (B) possible structure of nanoparticles comprising two different constituents.

In situ ASAXS studies of electrochemical energy devices

The high flux and strong penetration power of synchrotron X-rays make it feasible to study supported active nanoparticles in working electrochemical energy devices (e.g., fuel cells, supercapacitors, batteries) by *in situ* ASAXS. For example, *in situ* ASAXS studies near the

Figure 6. Characterization of core-shell micelles of poly(ethylene glycol)-*block*-poly(partially benzyl-esterified aspartic acid) loaded with tetrabromocathecol (TBC) molecules, or PEAB-Br*x* (*x* = weight percentage of TBC loading). (A) Typical small-angle X-ray scattering (SAXS) profiles of low-concentration PEAB-Br*x* micelles recorded using X-ray at an energy of 12.4 keV. Theoretical fitting results (unbroken red curves) were obtained using a core-shell model. (B) Top frame: Comparison of the SAXS profiles of PEAB-Br2.4 micelles at high concentration (40 mg/ml) and low concentration (extrapolated zero), showing the significant difference at low q. Bottom frame: Division of the profile at 40 mg/ml by that at zero concentration gave the concentration-dependent structure factor (blue dots). At high $q > 0.5$, the structural factor $S(q)$ was set to 1 (red symbols). (C) SAXS profiles for 40 mg/ml PEAB-Br2.4 micelles recorded at several X-ray energies near the absorption edge of Br (left) and the same profiles after correction with the structure factor shown in the bottom frame of (B). The values in the legend represent the energy difference of the X-rays with respect to the absorption edge of Br. (D) Typical SAXS profile of PEAB-Br2.4 micelles (black symbols) and the resonant term of Br (blue symbols). Theoretical curves were calculated from hard-sphere models with dispersity (unbroken red and green curves). (E) Schematic illustration of a PEAB-Br2.4 micelle particle highlighting the uniform distribution of TBC molecules in the core and infiltration of TBC molecules into the shell in the vicinity of the core/shell interface. Adapted from [48].

absorption edges of catalyst metal nanoparticles on conductive supports (e.g., carbon and conductive oxides) in fuel cells reveal the time-dependent variation of particle size distribution (PSD) and structural variation [66–70]. Correlating the variations with the real-time fuel cell performance is helpful to understand the structure–property relationship (i.e., the dependence of electrochemical catalytic activity on the structure of catalyst metal nanoparticles). Other examples include studies on the morphological changes of carbon-coated TiO_2 anatase nanoparticles in working sodium-ion batteries [71] and the spatial distribution of Rb^+ ions in mesoporous/nanoporous carbon electrodes that are ideal for electrochemical capacitors [72].

Concluding remarks

The rapid development of synchrotron facilities allows access by more researchers, promoting the advancement of emerging ASAXS in research areas of materials chemistry, as summarized in this review. ASAXS inherits the merit of SAXS in understanding the geometrical structures (or so-called 3D imaging) of interesting molecules/nanoparticles by analysis of the signals of a large number of objects. The averaged statistic results complement those recorded with localized characterization techniques (e.g., transmission electron microscopy). Anomalous measurement offers the capability of determining element-specific structures in composite samples, providing more comprehensive signals to understand the correlation of the properties/functionality of the samples with their structure and chemical composition. The strong penetration power of high-flux synchrotron X-rays, the ambient operation environment, and the large working space facilitate the use of *in situ* ASAXS to study interesting materials in working devices under real conditions. Immediate challenges (see Outstanding questions) need to be tackled to enable deconvoluted element-specific SAXS profiles with high fidelity from ASAXS measurements of composite samples. The challenges originate from the structural distribution (variation) of individual molecules/nanoparticles in a sample and the minor variations of SAXS signals at different X-ray energies, both of which make it challenging to analyze the ASAXS data. Although simple subtraction of the SAXS signal at the non-resonant energy from that at the resonant energy is sometimes used to derive the SAXS profile of the resonant element [67], ignorance of the contribution of cross-term between the resonant element and non-resonant elements usually leads to inaccurate (or even misleading) results. Continuing development of data-processing protocols will promote applications of ASAXS and *in situ* ASAXS for discoveries in materials chemistry.

Acknowledgments

This study is supported by the National Science Foundation of United States under NSF award 2002960.

Declaration of interests

The author declares no interests.

References

1. Li, T. *et al.* (2016) Small angle X-ray scattering for nanoparticle research. *Chem. Rev.* 116, 11128–11180
2. Putnam, C.D. *et al.* (2007) X-ray solution scattering (SAXS) combined with crystallography and computation: defining accurate macromolecular structures, conformations and assemblies in solution. *Q. Rev. Biophys.* 40, 191–285
3. Svergun, D.I. (1992) Determination of the regularization parameter in indirect-transform methods using perceptual criteria. *J. Appl. Crystallogr.* 25, 495–503
4. Glatter, O. and Kratky, O. (1982) *Small angle X-ray scattering*, Academic Press
5. Fritz, G. and Glatter, O. (2006) Structure and interaction in dense colloidal systems: evaluation of scattering data by the generalized indirect Fourier transformation method. *J. Phys. Condens. Matter* 18, S2403–S2419
6. Chacón, P. *et al.* (1998) Low-resolution structures of proteins in solution retrieved from X-ray scattering with a genetic algorithm. *Biophys. J.* 74, 2760–2775
7. Svergun, D.I. (1999) Restoring low resolution structure of biological macromolecules from solution scattering using simulated annealing. *Biophys. J.* 76, 2879–2886
8. Svergun, D.I. *et al.* (2001) Determination of domain structure of proteins from X-ray solution scattering. *Biophys. J.* 80, 2946–2953
9. Walther, D. *et al.* (2000) Reconstruction of low-resolution three-dimensional density maps from one-dimensional small-angle X-ray solution scattering data for biomolecules. *J. Appl. Crystallogr.* 33, 350–363
10. Sun, Y. *et al.* (2017) Quantitative 3D evolution of colloidal nanoparticle oxidation in solution. *Science* 356, 303–307

Outstanding questions

The statistics feature of SAXS and ASAXS measurements over many molecules/nanoparticles makes it challenging to use a single structure model to fit the SAXS profiles when the molecules/nanoparticles are not uniform in size. How could the contribution of the dimensional nonuniformity be considered to accurately fit the measured SAXS profiles with a proposed structure model?

What is crucial to increase the difference of recorded scattering intensity at different energies presented in the right matrix $\boldsymbol{y}$ of Equation 10 to suppress the measurement uncertainty (i.e., instrumental noise)? Carefully choosing the energies near the X-ray absorption edge of a resonant element might be a possible approach to maximize its anomalous effect and minimize the energy dependence of the non-resonant elements in a composite sample.

The linear simultaneous equation of Equation 10 becomes an 'ill-conditioned' problem when the solution is very sensitive to the values of the coefficient matrix $\boldsymbol{X}$. How can the problem be solved to deconvolute the element-specific SAXS profiles (i.e., matrix $\boldsymbol{\beta}$) from ASAXS measurements (i.e., matrix $\boldsymbol{y}$)?

The SAXS profiles of molecules/nanoparticles have been used to reconstruct their physical 3D geometries using *ab initio* determination protocols, in which an appropriate assembly of beads or dummy atoms renders the molecules/nanoparticles. Will it be feasible to use the element-specific SAXS profiles deconvoluted from ASAXS measurements to reconstruct the element-specific 3D geometries for composite samples? Success will potentially lead to a new imaging technique with chemical specificity, or so-called ASAXS imaging.

Is it possible to develop a general protocol including data processing, model fitting, and geometrical reconstruction that can be integrated with ASAXS measurements? Such a development will benefit the application of *in situ* ASXSA in a wide range of materials chemistry research, particularly requiring high temporal resolutions.

11. Brennan, S. and Cowan, P.L. (1992) A suite of programs for calculating X-ray absorption, reflection, and diffraction performance for a variety of materials at arbitrary wavelengths. *Rev. Sci. Instrum.* 63, 850–853
12. Sztucki, M. *et al.* (2012) Anomalous small-angle X-ray scattering from charged soft matter. *Eur. Phys. J. Spec. Top.* 208, 319–331
13. Stuhrmann, H.B. (1985) Resonance scattering in macromolecular structure research. *Adv. Polym. Sci.* 67, 123–163
14. Balyuzi, H. (1975) Analytic approximation to incoherently scattered X-ray intensities. *Acta Crystallogr. A* 31, 600–602
15. Hoell, A. *et al.* (2020) Crystallization of BaF_2 from droplets of phase separated glass – evidence of a core–shell structure by ASAXS. *CrystEngComm* 22, 5031–5039
16. Hoell, A. *et al.* (2014) ASAXS study of CaF_2 nanoparticles embedded in a silicate glass matrix. *J. Appl. Crystallogr.* 47, 60–66
17. Raghuwanshi, V.S. *et al.* (2015) Structral analysis of Fe–Mn–O nanoparticles in glass ceramics by small angle scattering. *J. Solid State Chem.* 222, 103–110
18. Raghuwanshi, V.S. *et al.* (2014) Crystallization of $ZrTiO_4$ nanocrystals in lithium-alumino-silicate glass ceramics: anomalous small-angle X-ray scattering investigation. *Cryst. Growth Des.* 14, 2838–2845
19. Revenant, C. (2018) Anomalous grazing-incidence small-angle X-ray scattering of Ga_2O_3-based nanoparticles. *J. Appl. Crystallogr.* 51, 436–445
20. Revenant, C. *et al.* (2015) Self-organized nanoclusters in solution-processed mesoporous In–Ga–Zn–O thin films. *Chem. Commun.* 51, 1218–1221
21. Huang, Y.-C. *et al.* (2020) Structural evolution and mechanism of strain glass transition in $Ti_{48.7}Ni_{51.3}$ shape memory alloy studied by anomalous small-angle X-ray scattering. *Sci. Rep.* 10, 9402
22. Okuda, H. *et al.* (2019) Two dimensional anomalous small-angle scattering measurements at the Mg *K* absorption edge for nanostructure analysis in concentrated Al–Mg alloys. *Appl. Phys. Express* 12, 075503
23. Okuda, H. *et al.* (2016) Realization of two-dimensional anomalous small-angle scattering of Al alloys at the *K* absorption edge of Al. *J. Appl. Crystallogr.* 49, 1803–1805
24. Chehaidar, A. (2015) Anomalous small-angle X-ray scattering of nanoporous two-phase atomistic models for amorphous silicon–germanium alloys. *Mater. Charact.* 107, 54–62
25. Kumada, T. *et al.* (2020) Anomalous small-angle X-ray scattering (ASAXS) study of irradiation-induced nanostructure change in Fe-ion beam irradiated oxide dispersion-strengthened (ODS) steel. *J. Nucl. Mater.* 528, 151890
26. Dumont, M. *et al.* (2014) Chemical composition of nano-phases studied by anomalous small-angle X-ray scattering: application to oxide nano-particles in ODS steels. *Mater. Charact.* 87, 138–142
27. Oba, Y. *et al.* (2019) Characterization of $BaZrO_3$ nanocolumns in Zr-added (Gd,Y)$Ba_2Cu_3O_x$ superconductor tape by anomalous small-angle X-ray scattering. *Supercond. Sci. Technol.* 32, 055011
28. Paskevicius, M. *et al.* (2016) Cyclic stability and structure of nanoconfined Ti-doped $NaAlH_4$. *Int. J. Hydrog. Energy* 41, 4159–4167
29. Karimi, F. *et al.* (2015) Structural and kinetic investigation of the hydride composite $Ca(BH_4)_2$ + MgH_2 system doped with NbF_5 for solid-state hydrogen storage. *Phys. Chem. Chem. Phys.* 17, 27328–27342
30. Karimi, F. *et al.* (2014) Structural analysis of calcium reactive hydride composite for solid state hydrogen storage. *J. Appl. Crystallogr.* 47, 67–75
31. Chen, J. *et al.* (2021) Accurate determination of the quantity and spatial distribution of counterions around a spherical macroion. *Angew. Chem. Int. Ed.* 60, 5833–5837
32. Radnik, J. *et al.* (2019) Identifying the location of Cu ions in nanostructured SAPO-5 molecular sieves and its impact on the redox properties. *RSC Adv.* 9, 6429–6437
33. Lages, S. *et al.* (2013) SAXS and ASAXS on dilute sodium polyacrylate chains decorated with lead ions. *Macromolecules* 46, 3570–3580
34. Goerigk, G. *et al.* (2016) Systematic limitations in concentration analysis via anomalous small-angle X-ray scattering in the small structure limit. *Polymers* 8, 85
35. Michels, R. *et al.* (2014) Coaggregation of two anionic azo dyestuffs: a combined static light scattering and small-angle X-ray scattering study. *J. Phys. Chem. B* 118, 7618–7629
36. Horkay, F. *et al.* (2018) Ionic effects in semi-dilute biopolymer solutions: a small angle scattering study. *J. Chem. Phys.* 149, 163312
37. Sushko, M.L. *et al.* (2016) The role of correlation and solvation in ion interactions with B-DNA. *Biophys. J.* 110, 315–326
38. Guéron, M. *et al.* (2016) Studies of the B–Z transition of DNA: the temperature dependence of the free-energy difference, the composition of the counterion sheath in mixed salt, and the preparation of a sample of the 5′-d[T-(m5C-G)12-T] duplex in pure B-DNA or Z-DNA form. *Biopolymers* 105, 369–384
39. Meisburger, S.P. *et al.* (2015) Determining the locations of ions and water around DNA from X-ray scattering measurements. *Biophys. J.* 108, 2886–2895
40. Horkay, F. *et al.* (2015) Effect of calcium/sodium ion exchange on the osmotic properties and structure of polyelectrolyte gels. *Proc. Inst. Mech. Eng. H J. Eng. Med.* 229, 895–904
41. Nguyen, H.T. *et al.* (2014) Accurate small and wide angle X-ray scattering profiles from atomic models of proteins and nucleic acids. *J. Chem. Phys.* 141, 22D508
42. Ingham, B. *et al.* (2018) Elemental fingerprinting of mineral species in iron-fortified milk: anomalous small-angle X-ray scattering and resonant soft X-ray scattering studies. *J. Synchrotron Radiat.* 25, 1106–1112
43. Fairclough, R.H. and Lee, T.E. (2017) Structural insights from membrane small-angle X-ray diffraction with anomalous X-ray scattering. In *Modern tools of biophysics* (Jue, T., ed.), pp. 65–80, Springer
44. Zettl, T. *et al.* (2016) Absolute intramolecular distance measurements with Ångstrom-resolution using anomalous small-angle X-ray scattering. *Nano Lett.* 16, 5353–5357
45. Pinfield, V.J. and Scott, D.J. (2014) Anomalous small angle X-ray scattering simulations: proof of concept for distance measurements for nanoparticle-labelled biomacromolecules in solution. *PLoS One* 9, e95664
46. Sakou, M. *et al.* (2013) Study of the internal structure of polymer micelles by anomalous small-angle X-ray scattering at two edges. *J. Appl. Crystallogr.* 46, 1407–1413
47. Manet, S. *et al.* (2015) Structure of bolaamphiphile sophorolipid micelles characterized with SAXS, SANS, and MD simulations. *J. Phys. Chem. B* 119, 13113–13133
48. Sanada, Y. *et al.* (2013) Hydrophobic molecules infiltrating into the poly(ethylene glycol) domain of the core/shell interface of a polymeric micelle: evidence obtained with anomalous small-angle X-ray scattering. *J. Am. Chem. Soc.* 135, 2574–2582
49. Sasaki, S. *et al.* (2018) Elucidation of spatial distribution of hydrophobic aromatic compounds encapsulated in polymer micelles by anomalous small-angle X-ray scattering. *Polymers* 10, 180
50. Nakanishi, R. *et al.* (2016) Anomalous small-angle X-ray scattering study on the spatial distribution of hydrophobic molecules in polymer micelles. *Polym. J.* 48, 801–806
51. Hamamoto, H. *et al.* (2021) Analysis of homopolymer distribution in a polymer blend thin film by anomalous grazing incidence small-angle X-ray scattering at the bromine *K*-edge. *Macromolecules* 54, 488–498
52. Humbert, S. *et al.* (2021) ASAXS study of the influence of sulfidation conditions and organic additives on sulfide slabs multiscale organization. *J. Catal.* 395, 412–424
53. Weber, C. *et al.* (2015) Electroless preparation and ASAXS microstructural analysis of pseudocapacitive carbon manganese oxide supercapacitor electrodes. *Langmuir* 31, 782–788
54. Rumancev, C. *et al.* (2017) Morphological analysis of cerium oxide stabilized nanoporous gold catalysts by soft X-ray ASAXS. *RSC Adv.* 7, 45344–45350
55. Binninger, T. *et al.* (2015) Particle-support interferences in small-angle X-ray scattering from supported-catalyst materials. *Phys. Rev. Appl.* 3, 024012
56. Vogtt, K. *et al.* (2013) Anomalous small-angle x-ray scattering from mesoporous noble metal catalysts. *Colloid Polym. Sci.* 291, 2163–2171
57. Georgieva, J. *et al.* (2015) Pt(Ni) electrocatalysts for methanol oxidation prepared by galvanic replacement on TiO_2 and TiO_2–C powder supports. *J. Electroanal. Chem.* 754, 65–74

58. Høydalsvik, K. *et al.* (2014) Morphology chages of Co catalyst nanoparticles at the onset of Fischer–Tropsch synthesis. *J. Phys. Chem. C* 118, 2399–2407
59. Allen, A.J. *et al.* (2014) Evolution of electrochemical interfaces in solid oxide fuel cells (SOFC): a Ni and Zr resonant anomalous ultra-small-angle X-ray scattering study with elemental and spatial resolution across the cell assembly. *RSC Adv.* 4, 4676–4690
60. Kehres, J. *et al.* (2015) Reduction of a Ni/spinel catalyst for methane reforming. *J. Phys. Chem. C* 119, 1424–1432
61. Haas, S. *et al.* (2013) Cascade catalysis of highly active bimetallic Au/Pd nanoclusters: structure–function relationship investigation using anomalous small-angle X-ray scattering and UV–Vis spectroscopy. *J. Appl. Crystallogr.* 46, 1353–1360
62. Helgadottir, I. *et al.* (2014) Ru-core/Cu-shell bimetallic nanoparticles with controlled size formed in one-pot synthesis. *Nanoscale* 6, 14856–14862
63. Ludescher, L. *et al.* (2019) Impact of crystal structure and particles shape on the photoluminescence intensity of CdSe/CdS core/shell nanocrystals. *Front. Chem.* 6, 672
64. Krycka, K.L. *et al.* (2013) Resolving material-specific structures within Fe_3O_4|γ-Mn_2O_3 core|shell nanoparticles using anomalous small-angle X-ray scattering. *ACS Nano* 7, 921–931
65. Yarema, M. *et al.* (2017) Mapping the atomistic structure of graded core/shell colloidal nanocrystals. *Sci. Rep.* 7, 11718
66. Gilbert, J.A. *et al.* (2012) *In situ* anomalous small-angle X-ray scattering studies of platinum nanoparticle fuel cell electrocatalyst degradation. *J. Am. Chem. Soc.* 134, 14823–14833
67. Tuaev, X. *et al.* (2013) *In situ* study of atomic structure transformations of Pt–Ni nanoparticle catalysts during electrochemical potential cycling. *ACS Nano* 7, 5666–5674
68. Gilbert, J.A. *et al.* (2015) In-operando anomalous small-angle X-ray scattering investigation of Pt_3Co catalyst degradation in aqueous and fuel cell environments. *J. Electrochem. Soc.* 162, F1487–F1497
69. Binninger, T. *et al.* (2016) Electrochemical flow-cell setup for *in situ* X-ray investigations. *J. Electrochem. Soc.* 163, H906–H912
70. Binninger, T. *et al.* (2017) Stabilization of Pt nanoparticles due to electrochemical transistor switching of oxide support conductivity. *Chem. Mater.* 29, 2831–2843
71. Greco, G. and Passerini, S. (2020) Sodium induced morphological changes of carbon coated TiO_2 anatase nanoparticles – high-performance materials for Na-ion batteries. *MRS Adv.* 5, 2221–2229
72. Koczwara, C. *et al.* (2019) Towards real-time ion-specific structural sensitivity in nanoporous carbon electrodes using in situ anomalous small-angle X-ray scattering. *ACS Appl. Mater. Interfaces* 11, 42214–42220